

USING THE NAVIER-CAUCHY EQUATION FOR MOTION ESTIMATION IN DYNAMIC IMAGING

B.N. HAHN*, M.-L. KIENLE-GARRIDO*, C. KLINGENBERG†, AND S. WARNECKE†

Abstract. Tomographic image reconstruction is well understood if the specimen being studied is stationary during data acquisition. However, if this specimen changes its position during the measuring process, standard reconstruction techniques can lead to severe motion artefacts in the computed images. Solving a dynamic reconstruction problem therefore requires to model and incorporate suitable information on the dynamics in the reconstruction step to compensate for the motion.

Many dynamic processes can be described by partial differential equations which thus could serve as additional information for the purpose of motion compensation. In this article, we consider the Navier-Cauchy equation which characterizes small elastic deformations and serves, for instance, as a simplified model for respiratory motion. Our goal is to provide a proof-of-concept that by incorporating the deformation fields provided by this PDE, one can reduce the respective motion artefacts in the reconstructed image. To this end, we solve the Navier-Cauchy equation prior to the image reconstruction step using suitable initial and boundary data. Then, the thus computed deformation fields are incorporated into an analytic dynamic reconstruction method to compute an image of the unknown interior structure. The feasibility is illustrated with numerical examples from computerized tomography.

Key words. Dynamic inverse problems, Tomography, Motion estimation, Elasticity equation, Dynamics in Lagrangian coordinates

AMS subject classifications. 44A12, 65R32, 92C55, 74B05

1. Introduction. Tomographic imaging modalities represent a well-known application of the theory of inverse problems. If the specimen is stationary during the data collection, the reconstruction process is well understood for most imaging systems [36]. A dynamic behaviour of the object during measurement, however, results in inconsistent data, and standard reconstruction techniques derived under the stationary assumption lead to severe motion artefacts in the computed images [13, 31, 42]. This affects medical applications, for instance due to respiratory motion, as well as non-destructive testing while imaging driven liquid fronts for oil recovery studies [3] or while performing elasticity experiments during the scan to determine material parameters [25].

An intuitive approach for the case of few but consistent data would be to consider a quasi-static framework. However, this is only applicable if the object motion is sufficiently slow compared to the overall data acquisition time or if the motion is periodic. Solving the dynamic reconstruction problem in general requires to model and incorporate dynamical prior information within the reconstruction step. For individual imaging modalities like computerized tomography, magnetic resonance imaging or positron emission tomography, several methods of this type have been proposed in the literature, based on rebinning or gating the data [15, 33, 46], a variational formulation [6, 14, 32, 37], exact analytic methods [11, 12, 20], iterative procedures [2, 24] or approximate inversion formulas [17, 26, 27]. Further, regularization techniques developed in the general context of dynamic linear inverse problems [8, 16, 29, 40, 41] have been successfully applied to imaging problems.

The most efficient way to compensate for the dynamics is to model and incorporate

*Department of Mathematics, University of Stuttgart (bernadette.hahn@imng.uni-stuttgart.de, melina-loren.kienle-garrido@imng.uni-stuttgart.de).

†Department of Mathematics, University of Würzburg (klingen@mathematik.uni-wuerzburg.de, sandra.warnecke@mathematik.uni-wuerzburg.de).

the motion prior in form of a deformation map Φ which describes the trajectory of the particles in the interior of the object over time. In general, such deformation fields are a priori unknown and have to be extracted from the measured data. Typically, parametrized motion models are employed, i.e. only a few unknown parameters need to be estimated, either via additional measurements [2, 11, 34, 39] or directly from the recorded tomographic data. In computerized tomography, for instance, they can be determined by detecting traces of nodal points in the sinogram [17, 33]. For global rotations and translations, an estimation procedure using data consistency conditions is proposed in [48]. Iterative procedures are, for example, based on edge entropy [28], or perform estimation and reconstruction step simultaneously [45].

Alternatively, the dynamics can be characterized in terms of velocity fields between consecutive image frames. The intensity variations in the image sequence are then linked to the underlying velocity field by the optical flow constraint, based on the brightness constancy assumption. Recovering both velocity fields and image frames from the measured data simultaneously requires solving non-convex optimization problems of extremely large size [4, 5].

In this article, we pursue another approach. Many dynamic processes can be described by partial differential equations, and thus, their (numerical) solution could provide the required deformation fields. More precisely, we consider in the following the Navier-Cauchy equation, representing linear elasticity. In applications in radiotherapy treatment planning, the respective conservation laws are employed to model respiratory motion [47].

To reduce the overall complexity and to provide a proof-of-concept that such motion priors can compensate for the dynamics, we suggest to decouple both tasks for the study in this article. Based on the provided results, the study of the joint parameter identification problem will then be subject to future work.

In Section 2, we recall the mathematical model of dynamic imaging and present the general motion compensation strategy from [18] in the mass preserving case which assumes that the motion is known. We then derive our elastic motion model based on conservation laws in Section 3. The respective model in particular requires prescribed initial and boundary data. Therefore, we discuss suitable choices which are feasible regarding practical applications. The numerical calculation of the deformation fields is studied in Section 4. Finally, the potential of the motion model for the purpose of motion compensation is illustrated in Section 5 at the example of computerized tomography, combining the numerically computed deformation fields with our dynamic reconstruction strategy. We conclude with an outlook to expand the suggested approach towards determining an unperturbed image and the deformation fields simultaneously via a joint parameter identification problem.

2. Models and reconstruction strategies in dynamic imaging. In this section, we introduce the mathematical framework to formulate and address the problem of dynamic image reconstruction. In particular, we will consider the two-dimensional case throughout the article. Further, since the motion estimation approach via the Navier-Cauchy equation is not restricted to a particular imaging modality, we want to present the motion compensation strategy in a framework covering many different modalities. A detailed introduction can be found for instance in [16, 18].

We start by deriving the model of the stationary setting. To be more intuitive, we first consider the example of computerized tomography (CT). In CT, X-ray beams are transmitted through the specimen of interest to a detector where the intensity loss of the X-rays is recorded. Is the intensity at the source position denoted by I_0 and the intensity

at the detector position by I_1 , then the CT-measurement for this particular configuration is given by $\log\left(\frac{I_0}{I_1}\right)$. In particular, the radiation source needs to rotate around the object to capture information from different angles of view. Due to this rotation, the data acquisition takes a considerable amount of time. The mathematical model for this imaging process is given by the Radon transform

$$(2.1) \quad (\mathcal{R}h)(t, y) = \int_{\mathbb{R}^2} h(x) \delta(y - x^T \theta(t)) dx, \quad (t, y) \in [0, 2\pi] \times \mathbb{R},$$

which integrates h along the straight lines $\{x \in \mathbb{R}^2 : x^T \theta(t) = y\}$, i.e. along the path of the emitted X-rays. Every source position corresponds to one time instance, in particular, the unit vector $\theta(t) = (\cos(t), \sin(t))^T$ characterizes the source position at time instance t , while y denotes the affected detector point, and δ stands for the delta distribution. The goal is then to recover h , the linear attenuation coefficient of the studied specimen, from measurements $g(t, y) = (\mathcal{R}h)(t, y)$ with $(t, y) \in [0, 2\pi] \times \mathbb{R}$. Using the Fourier transform of δ , we further obtain the equivalent representation

$$(\mathcal{R}h)(t, y) = \int_{\mathbb{R}} \int_{\mathbb{R}^2} (2\pi)^{-1/2} e^{i\sigma(y - x^T \theta(t))} h(x) dx d\sigma.$$

Besides CT, many imaging modalities in the stationary setting can be modeled mathematically by a linear operator which integrates the searched-for quantity along certain manifolds, for instance along circles, respectively spheres, in SONAR or photoacoustic tomography. Thus, we consider in the following a more general framework, namely model operators of type

$$(2.2) \quad \mathcal{A}h(t, y) = \int_{\mathbb{R}} \int_{\Omega_x} h(x) a(t, y, x) e^{i\sigma(y - H(t, x))} dx d\sigma, \quad (t, y) \in \mathbb{R}_T \times \Omega_y,$$

where Ω_x and Ω_y denote open subsets of \mathbb{R}^2 and \mathbb{R} , respectively, $\mathbb{R}_T \subset \mathbb{R}$ represents an open time interval covering the time required for the measuring process, $a \in C^\infty(\mathbb{R}_T \times \Omega_y \times \Omega_x)$ is a weight function and $H : \mathbb{R}_T \times \mathbb{R}^2 \rightarrow \mathbb{R}$ characterizes the manifold we are integrating over.

With this observation model, we can formulate the associated inverse problem: Determine h from measured data

$$(2.3) \quad g(t, y) = \mathcal{A}h(t, y), \quad (t, y) \in \mathbb{R}_T \times \Omega_y.$$

The component t of the data variable expresses the time-dependency of the data collection process. The searched-for quantity h itself, however, is independent of time, i.e. (2.3) corresponds to a *static* image reconstruction problem. We refer to equation (2.3) also as *static inverse problem*.

2.1. The mathematical model of dynamic imaging. Now, we consider the dynamic case, i.e. the investigated object changes during collection of the data and is therefore characterized by a time-dependent function $f : \mathbb{R}_T \times \mathbb{R}^2 \rightarrow \mathbb{R}$. For a fixed time, we abbreviate $f_t := f(t, \cdot)$, i.e. f_t represents the state of the object at time instance t . Then, the inverse problem of the dynamic scenario reads

$$(2.4) \quad \mathcal{A}^{dyn} f(t, y) = g(t, y)$$

with the dynamic operator $\mathcal{A}^{dyn} f(t, y) := \mathcal{A} f_t(t, y)$. In particular, only measurements $g(t, \cdot)$ for a single time instance encode information about the state f_t , which is typically not sufficient to fully recover f_t . In CT, only line integrals in one particular direction would be available for the reconstruction of f_t , which is well known to be insufficient. Thus, additional information about the dynamic behavior need to be incorporated in order to solve dynamic inverse problems.

The dynamic behaviour of the object can be considered to be due to particles which change position in a fixed coordinate system of \mathbb{R}^2 . This physical interpretation of object movement can then be incorporated into a mathematical model $\Phi : \mathbb{R}_T \times \mathbb{R}^2 \rightarrow \mathbb{R}^2$, where $\Phi(0, x) = x$, i.e. we consider f_0 as reference state, and $\Phi(t, x)$ denotes the position at time t of the particle initially at x . For fixed $t \in \mathbb{R}_T$, we write $\Phi_t x := \Phi(t, x)$ to simplify the notation. Motivated by medical applications, where no particle is lost or added and two particles cannot move to the same position at the same time, Φ_t is assumed to be a diffeomorphism for all $t \in \mathbb{R}_T$. Thus, a particle $x \in \mathbb{R}^2$ at time t is at position $\Phi_t^{-1} x$ in the reference state, see Figure 1. A description of this motion model can also be found, for instance, in [16, 26, 27].

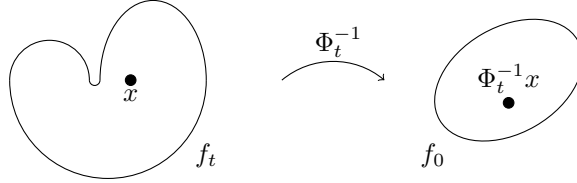


Figure 1: The mapping Φ_t^{-1} correlates the state f_t at time t to the reference state f_0 at the initial time.

Using this motion model and the initial state function f_0 , we find the state of the object at time instance t to be

$$(2.5) \quad f(t, x) = f_0(\Phi_t^{-1}x) |\det D\Phi_t^{-1}x|$$

by taking into account that mass shall be preserved.

Inserting the property (2.5) in the definition of the dynamic forward operator \mathcal{A}^{dyn} , we obtain an operator \mathcal{A}_Φ for the initial state function, namely

$$(2.6) \quad \mathcal{A}_\Phi f_0(t, y) := \mathcal{A}(|\det D\Phi_t^{-1}(\cdot)| (f_0 \circ \Phi_t^{-1}))(t, y).$$

Remark 2.1. In our previous work [16, 17, 21], we considered the intensity preserving model

$$f(t, x) = f_0(\Phi_t^{-1}x),$$

i.e. each particle keeps its initial intensity over time. Although this does not alter the nature of our reconstruction algorithm, we insist here on the mass preserving case to be consistent with the conservation laws employed in Section 3 for the purpose of motion estimation and clinical applications. The mass preserving model is also considered, for instance, in [26, 27].

For a theoretical analysis, the motion model Φ is typically assumed to satisfy the following additional conditions, cf. [9, 19, 21, 38]:

- The map

$$(2.7) \quad x \mapsto \begin{pmatrix} H(t, \Phi_t x) \\ D_t H(t, \Phi_t x) \end{pmatrix}$$

is one-to-one for each t .

- It holds

$$(2.8) \quad \det \begin{pmatrix} D_x H(t, \Phi_t x) \\ D_x D_t H(t, \Phi_t x) \end{pmatrix} \neq 0$$

for all $x \in \mathbb{R}^2$ and all $t \in \mathbb{R}_T$.

Basically, these properties ensure that the object's motion does not result in trivial sampling schemes for f_0 . A detailed interpretation of these conditions can be found, for instance, in [21].

If the deformation fields Φ_t are known, the dynamic inverse problem (2.4) reduces to determining f_0 from the equation

$$(2.9) \quad \mathcal{A}_\Phi f_0 = g.$$

In [16, 18, 26], efficient algorithms have been developed to solve this task. The underlying strategy proposed in [18] is summarized in the following, before we introduce our PDE-based approach to determine the deformation fields Φ_t in Section 3 and combine both strategies to solve (2.9) when Φ_t are unknown.

2.2. Motion compensation algorithms. Throughout this section, we assume the motion Φ to be known and focus on solving (2.9). Under suitable assumptions on the phase function H , the linear integral operator \mathcal{A} from the underlying static case belongs to the class of *Fourier integral operators*. To define this type of operators, we first introduce the concepts of amplitude and phase function.

DEFINITION 2.2.

- Let $\Lambda \in C^\infty(\mathbb{R}_T \times \Omega_y \times \Omega_x \times \mathbb{R} \setminus \{0\})$ be a real-valued function with the following properties:
 1. Λ is positive homogeneous of degree 1 in σ , i.e. $\Lambda(t, y, x, r\sigma) = r\Lambda(t, y, x, \sigma)$ for every $r > 0$,
 2. both $(\partial_{(t,y)}\Lambda, \partial_\sigma\Lambda)$ and $(\partial_x\Lambda, \partial_\sigma\Lambda)$ do not vanish for all $(t, y, x, \sigma) \in \mathbb{R}_T \times \Omega_y \times \Omega_x \times \mathbb{R} \setminus \{0\}$,
 3. it holds $\partial_{(t,y,x)}(\frac{\partial\Lambda}{\partial\sigma}) \neq 0$ on the zero set

$$\Sigma_\Lambda = \{(t, y, x, \sigma) \in \mathbb{R}_T \times \Omega_y \times \Omega_x \times \mathbb{R} \setminus \{0\} : \partial_\sigma\Lambda = 0\}.$$

Then, Λ is called a non-degenerate phase function.

- Let $a \in C^\infty(\mathbb{R}_T \times \Omega_y \times \Omega_x \times \mathbb{R})$ satisfy the following property:
For every compact set $K \subset \mathbb{R}_T \times \Omega_y \times \Omega_x$ and for every $M \in \mathbb{N}$, there exists a $C = C(K, M) \in \mathbb{R}$ such that

$$\left| \frac{\partial^{n_1}}{\partial t^{n_1}} \frac{\partial^{n_2}}{\partial y^{n_2}} \frac{\partial^{n_3}}{\partial x_1^{n_3}} \frac{\partial^{n_4}}{\partial x_2^{n_4}} \frac{\partial^m}{\partial \sigma^m} a(t, y, x, \sigma) \right| \leq C(1 + |\sigma|)^{k-m}$$

for $n_1 + n_2 + n_3 + n_4 \leq M$, $m \leq M$, for all $(t, y, x) \in K$ and for all $\sigma \in \mathbb{R}$.
Then a is called an amplitude (of order k).

- Let Λ denote a non-degenerate phase function and let a be an amplitude (of order k). Then, the operator \mathcal{T} defined by

$$\mathcal{T}u(t, y) = \int u(x)a(t, y, x, \sigma)e^{i\Lambda(t, y, x, \sigma)}dx d\sigma, \quad (t, y) \in \mathbb{R}_T \times \Omega_y$$

is called a Fourier integral operator (FIO) (of order $k - 1/2$).

For more details and a more general definition see [22, 44].

In [18, 19], it was shown that under suitable smoothness conditions on Φ , the dynamic operator \mathcal{A}_Φ inherits the FIO property from its static counterpart \mathcal{A} .

THEOREM 2.3. *Let $\Phi \in C^\infty(\mathbb{R}_T \times \mathbb{R}^2)$ and let Φ_t be a diffeomorphism for every $t \in \mathbb{R}_T$. If the static operator \mathcal{A} from (2.2) is an FIO, the respective dynamic operator \mathcal{A}_Φ from (2.6) is an FIO as well.*

Fourier integral operators have specific properties that can be used to design efficient motion compensation strategies: They encode characteristic features of the object - the so-called *singularities* - in precise and well-understood ways.

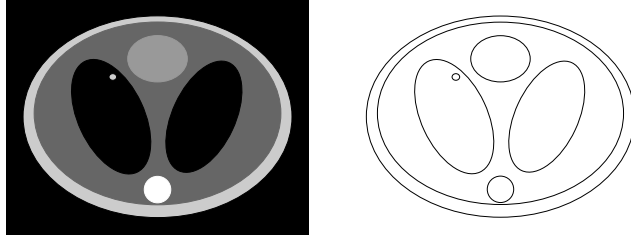


Figure 2: Initial state f_0 of a phantom (left) and its singularities (right).

Formally, singularities of a (generalized) function h correspond to the elements of the *singular support* $\text{supp}(h)$, which denotes the complement of the largest open set on which h is smooth. In imaging applications, where the searched-for quantity is typically piecewise constant (each value characterizing a particular material), the singularities correspond to the contours of h , see Figure 2.

The method for motion compensation from [18] is motivated by results on microlocal analysis, which address - among others - the question which singularities can be stably recovered from the data. The main idea is to use reconstruction operators of the form

$$(2.10) \quad \mathcal{L}_\Phi = \mathcal{B}_\Phi \mathcal{P}$$

on the data $g = \mathcal{A}_\Phi f_0$ with \mathcal{P} a *pseudodifferential operator* (typically acting on the spatial data variable y) and a *backprojection operator* \mathcal{B}_Φ which incorporates the information on the dynamic behavior.

DEFINITION 2.4. *a) An operator of the form*

$$\mathcal{P}g(t, s) = \int_{\mathbb{R}} \int_{\mathbb{R}} e^{i\sigma(s-y)} p(s, y, \sigma) g(t, y) dy d\sigma$$

with $|\sigma| \leq 1$ and amplitude p which is locally integrable for s, y in any compact set K is called pseudodifferential operator (PSIDO) (acting on the spatial data variable y).

b) The operator

$$\mathcal{B}_\Phi g(x) = \int_{\mathbb{R}_T} b(t, x) g(t, H(t, \Phi_t x)) dt, \quad x \in \mathbb{R}^2,$$

where $b(t, x)$ is a positive C^∞ -weight function on $\mathbb{R}_T \times \mathbb{R}^2$, is called backprojection operator associated to \mathcal{A}_Φ .

With these representations of \mathcal{B}_Φ and \mathcal{P} , the operator \mathcal{L}_Φ from (2.10) reads

$$(2.11) \quad \mathcal{L}_\Phi g(x) = \int_{\mathbb{R}_T} \int_{\mathbb{R}} \int_{\mathbb{R}} b(t, x) p(H(t, \Phi_t x), y, \sigma) g(t, y) e^{i\sigma(H(t, \Phi_t x) - y)} dy d\sigma dt.$$

Remark 2.5. a) Pseudodifferential operators constitute a special case of an FIO. A more general definition than the one given above can be found, for instance, in [30].
b) If we choose the weight $b(t, x) = a(t, H(t, \Phi_t), \Phi_t x)$ with the amplitude a of the underlying static operator \mathcal{A} , the respective backprojection operator \mathcal{B}_Φ corresponds to the dual operator of \mathcal{A}_Φ .

The following result forms the basis to our motion compensation method.

THEOREM 2.6. *Let $\Phi \in C^\infty(\mathbb{R}_T \times \mathbb{R}^2)$ and let $\Phi_t, t \in \mathbb{R}_T$ be diffeomorphisms that satisfy the conditions (2.7) and (2.8). Further, let $\mathcal{L}_\Phi = \mathcal{B}_\Phi \mathcal{P}$ be well-defined. Then, \mathcal{L}_Φ preserves the singularities of f_0 which are ascertained in the measured data.*

Proof. Since Φ is smooth and Φ_t is a diffeomorphism for each $t \in \mathbb{R}_T$ and since $\mathcal{L}_\Phi = \mathcal{B}_\Phi \mathcal{P}$ is well-defined for the PSIDO \mathcal{P} , Hypothesis 1 from [19] is fulfilled. Further conditions (2.7) and (2.8) are satisfied, which are the conditions (17) and (18) in [19]. Hence, Theorem 13 from [19] can be applied. This gives us

$$\text{ssup}(\mathcal{L}_\Phi f_0) \subset \text{ssup}(f_0) \cap \mathcal{V},$$

where $\text{ssup}(h)$ is the singular support of h , which is the set of singularities of h , for more information see [19]. Further \mathcal{V} is the set of visible singularities of f_0 or in other words of singularities of f_0 that are ascertained in the measured data. \square

Interpretation: Applying a reconstruction operator \mathcal{L}_Φ of type (2.10) provides an image showing the singularities of f_0 correctly, which are encoded by the dynamic data. In particular, no motion artefacts arise. Thus, the described approach provides in fact a motion compensation strategy. In particular, it can be easily implemented and the computational effort is comparable to the one of static reconstruction algorithms of type *filtered backprojection*. If an inversion formula of type $u = \mathcal{A}^* \mathcal{P}^{stat} \mathcal{A} u$ with a PSIDO \mathcal{P}^{stat} is known for the static case, then choosing the PSIDO $\mathcal{P} = \mathcal{P}^{stat}$ for the motion compensation strategy provides even a good approximation to the exact density values of f_0 [18]. In computerized tomography, such an inversion formula is known with \mathcal{P}^{stat} being the *Riesz potential* [35].

Remark 2.7. Although the ascertained singularities of f_0 are correctly reconstructed by \mathcal{L}_Φ , some additional artefacts might occur if the motion is non-periodic. This has been studied in detail for computerized tomography in [21] and for a more general class of imaging

problems in [19]. These artefacts would be caused by singularities encoded at beginning and end of the scanning and would spread along the respective integration curve. Nevertheless, this is an intrinsic property due to the nature of the dynamic problem and therefore does not impose a major restriction to our reconstruction approach. In particular, for periodic motion as in medical applications, such as respiratory motion, the data acquisition protocol could be adjusted to the breathing cycle to avoid this issue.

Since inverse problems are typically ill-posed, a regularization is required to determine $\mathcal{L}_\Phi g$ stably from the measured data $g = \mathcal{A}_\Phi f_0$. For our considered class of imaging problems, the ill-posedness is typically revealed by the growth of the symbol p in terms of σ . For instance, the amplitude of the Riesz potential arising in computerized tomography corresponds to $p(s, y, \sigma) = p(\sigma) = |\sigma|$, thus, amplifying the high frequencies of the data g . The inversion process can be stabilized by introducing a smooth low-pass filter e^γ , i.e. by considering

$$(2.12) \quad \mathcal{L}_\Phi^\gamma g(x) = \int_{\mathbb{R}_T} \int_{\mathbb{R}} \int_{\mathbb{R}} b(t, x) p(H(t, \Phi_t x), y, \sigma) e^\gamma(\sigma) g(t, y) e^{i\sigma(H(t, \Phi_t x) - y)} dy d\sigma dt$$

with $\gamma > 0$ instead of (2.11), see [18] for more details.

2.3. Reconstruction operator in dynamic CT. Since we will evaluate our motion estimation strategy in Section 5 at the example of computerized tomography, we want to state the respective motion compensation algorithm for this application explicitly.

As introduced in the beginning of this section, the mathematical model operator \mathcal{A} of the static case corresponds to the classical Radon transform \mathcal{R} , see (2.1), which is an FIO with amplitude $a(t, y, x) = (2\pi)^{-1/2}$ and phase function $\Lambda(t, y, x, \sigma) = \sigma(y - H(t, x))$, where $H(t, x) = x^T \theta(t)$ [30]. Thus, the associated dynamic backprojection operator \mathcal{B}_Φ with weight $b(t, x) = a(t, H(t, \Phi_t), \Phi_t x) = (2\pi)^{-1/2}$ reads

$$\mathcal{B}_\Phi g(x) = (2\pi)^{-1/2} \int_{\mathbb{R}_T} g(t, (\Phi_t x)^T \theta(t)) dt.$$

Choosing as PSIDO the Riesz potential with amplitude $p(s, y, \sigma) = |\sigma|$ and a low-pass filter e^γ , for instance the Gaussian, we obtain the dynamic reconstruction operator

$$\mathcal{L}_\Phi^\gamma g(x) = (2\pi)^{-1/2} \int_{\mathbb{R}_T} \int_{\mathbb{R}} \int_{\mathbb{R}} |\sigma| e^\gamma(\sigma) g(t, y) e^{i\sigma((\Phi_t x)^T \theta(t) - y)} dy d\sigma dt, \quad \gamma > 0,$$

which can be implemented in form of a *filtered backprojection* type algorithm, see [17].

3. Linear elastics. In this section and the following one, we will treat the task of motion estimation. While, for a global deformation, the dynamic behavior of the boundary can be observed externally, the deformation in the interior is a priori unknown. Since many dynamic processes can be mathematically described in terms of a partial differential equation (PDE), we propose to determine the deformation fields Φ_t by finding the solution of an appropriate PDE with suitable given initial and boundary data.

Since the deformation fields $\Phi_t, t \in \mathbb{R}_T$ describe the mapping from the initial/reference state to the current position, we choose the Lagrangian description for the PDE. Let $\Omega_x \subset \mathbb{R}^2$ denote the initial domain, i.e. Ω_x corresponds to the support of the initial state f_0 , and consequently, we choose Ω_x to be the reference configuration.

We require that $\Phi_t, t \in \mathbb{R}_T$ preserves its orientation meaning that $\det D\Phi(t, x) > 0$ for all $(t, x) \in \mathbb{R}_T \times \Omega_x$. Especially in medical applications, this assumption is sensible since it also states that the local ratio of the current and the initial volume never vanishes. [1]

The following definition links the current and the initial position.

DEFINITION 3.1. *The difference between the current and the initial position is called displacement $u(t, x) = \Phi(t, x) - x$ for all $(t, x) \in \mathbb{R}_T \times \Omega_x$.*

Our investigations are driven by medical applications. Having the cross section of a thorax in mind, we consider two spatial dimensions, which is reasonable under a plane strain assumption. The properties of respiratory motion shall then be reflected by adequate equations. Due to its periodic behavior, it is clear that occurring stresses do not cause any yielding. So we assume a linear relationship between stresses and strain which results in linear elasticity. In future work, we plan to consider more general stress-strain laws.

We consider this paper a proof-of-concept. Thus we insert Hooke's law in the general equation of conservation of momentum and arrive at the Navier-Cauchy equations in two spatial dimensions for $(t, x) \in \mathbb{R}_T \times \Omega_x$, see for reference [43]:

$$(3.1) \quad \hat{\rho} \frac{\partial^2 u_k}{\partial t^2} = \hat{v}_k + \mu \left(\frac{\partial^2 u_k}{\partial x_1^2} + \frac{\partial^2 u_k}{\partial x_2^2} \right) + (\lambda + \mu) \frac{\partial}{\partial x_k} \left(\frac{\partial u_1}{\partial x_1} + \frac{\partial u_2}{\partial x_2} \right) \quad \text{for } k = 1, 2.$$

These are two linear PDEs for the two unknown components u_1, u_2 of the displacement u with the following parameters:

- The density $\hat{\rho} = \rho(t, x) \det D\Phi(t, x)$ equals the initial density distribution $\hat{\rho} = \hat{\rho}(x) = \rho(0, x)$ due to the conservation of mass.
- The external volume forces are denoted by $\hat{v} = v(t, x) \det D\Phi(t, x)$, where $v : \mathbb{R}_T \times \Omega_x \rightarrow \mathbb{R}^2$ describes the volume force density.
- The Lamé-coefficients λ and μ specify the behavior of the material.

For a fully determined problem, we need the displacements at time $t = 0$ and their time derivatives as initial data

$$u(0, x) = \vartheta^0(x) \quad \text{and} \quad \frac{\partial}{\partial t} u(0, x) = \vartheta^1(x),$$

with some given $\vartheta^0, \vartheta^1 : \Omega_x \rightarrow \mathbb{R}^2$.

Also the behavior of the boundary needs to be known, more precisely a function $\psi : \mathbb{R}_T \times \Omega_x \rightarrow \mathbb{R}^2$ prescribing the evolution of the displacements on the boundary of the domain $\Gamma = \partial\Omega_x$:

$$u(t, x) = \psi(t, x) \quad \text{for } (t, x) \in \mathbb{R}_T \times \Gamma.$$

Solving the PDE we have introduced with given initial and boundary conditions corresponds to determining the displacement u , respectively the deformation Φ in the interior of the object from observations of the dynamic behavior of the object's boundary. This way we model the movement in the object's interior, which provides exactly the information about the motion needed for our motion compensation algorithm.

Under some regularity assumptions, existence and uniqueness of the solutions of the Navier-Cauchy equation (3.1) can be proven. If the initial data is C^∞ , solutions for the

initial value problem stay C^∞ , cf. [23]. Also for the initial-boundary value problem, there are existence and uniqueness results, cf. [7]. For appropriate boundary data ψ , regularity of the solutions does not get lost, and it can be shown that the solutions are diffeomorphisms, cf. [10]. In our numerical experiments in Section 5, the initial and boundary data is chosen so that the application of the motion compensation algorithm goes through.

In the following, we quickly discuss suitable initial and boundary data regarding our application in dynamic imaging. As mentioned before, a global motion can be observed externally, thus, we make the reasonable assumption that the boundary data $\psi(t, x)$, $(t, x) \in \mathbb{R}_T \times \Gamma$ are given. However, in practice, only discrete boundary data $\psi(t_n, x_{i,j})$, $n = 1, \dots, N$, $i = 1, \dots, I$, $j = 1, \dots, J$, $N, I, J \in \mathbb{N}$ will be available which might be even sparse with respect to the spatial component (i.e. I, J might be small) or corrupted by noise. This will be addressed in our numerical study in Section 5.

Since we are overall interested in a reconstruction of the initial state of the object and since we start with an undeformed configuration, the initial displacement data ϑ^0 and ϑ^1 will be set to zero.

Remark 3.2. According to (3.1), the Navier-Cauchy contains the initial density distribution $\hat{\rho}$ as parameter which is strongly linked to the quantity f_0 we would like to determine by our imaging modality (in particular, they share the same singularities). If we knew this parameter $\hat{\rho}$, we would already have full knowledge about the interior structure of the studied specimen. Thus, we cannot assume to know $\hat{\rho}$. Formally, we could formulate a joint motion estimation and image reconstruction approach, where we identify the parameter $\hat{\rho}$ of the PDE using the measurements from our imaging modality. However, to simplify the task for our proof-of-concept study, we propose another approach. In order to decouple the tasks of motion estimation via the Navier-Cauchy equation and dynamic image reconstruction, we use for the solution of the PDE a simplified prior instead of the exact density distribution $\hat{\rho}$. This is discussed in more detail in Section 5.

Remark 3.3. In this paper, we use the Navier-Cauchy equation to approximate the moving body. Using data at the boundary we deduce the motion of the whole body. For this we need to fix parameters of the Navier Cauchy PDE plus fix initial data. This is done by an informed guess (cf. the discussions in Section 4 and 5). Even with these approximations we find promising results in our numerical experiments, see Section 5. In future work, more elaborated PDEs are going to be considered in order to capture further details of the body's motion.

4. Numerical solution of the Navier-Cauchy equation. We divide the given time period $t \in \mathbb{R}_T$ into equidistant intervals and call the time steps $t_n = n \cdot \Delta t$. We choose a Cartesian grid (not necessarily uniform) so that the discrete boundary lies on the continuous boundary, see Figure 4. Using central finite differences of second order for the discretization of the Navier-Cauchy equation (3.1), we obtain an explicit numerical scheme. We have chosen finite difference for our proof-of-concept study. For future studies, we plan to use a more elaborated numerical method.

We denote $x_{i,j} = ((x_1)_i, (x_2)_j) = (x_i, y_j)$, $(u_k)_{i,j}^n = u_k(t_n, x_{i,j})$ for $k = 1, 2$, $\rho_{i,j}^0 = \hat{\rho}(x_{i,j})$, $\hat{v}_{i,j}^n = \hat{v}(t_n, x_{i,j})$, $\Delta x_i = x_{i+1} - x_i$ and $\Delta y_j = y_{j+1} - y_j$. Then the scheme reads

exemplary for the first component $k = 1$

$$\begin{aligned}
(u_1)_{i,j}^{n+1} &= \frac{\Delta t^2}{\rho_{i,j}^0} \hat{v}_{i,j}^n - (u_1)_{i,j}^{n-1} + 2 \left[1 - \frac{2\Delta t^2}{\rho_{i,j}^0} \left(\frac{\mu}{\Delta y_j^2 + \Delta y_{j-1}^2} + \frac{\lambda + 2\mu}{\Delta x_i^2 + \Delta x_{i-1}^2} \right) \right] (u_1)_{i,j}^n \\
&+ \frac{\Delta t^2}{\rho_{i,j}^0} \frac{2(\lambda + 2\mu)}{\Delta x_i^2 + \Delta x_{i-1}^2} \left[\left(1 - \frac{\Delta x_i - \Delta x_{i-1}}{\Delta x_i + \Delta x_{i-1}} \right) (u_1)_{i+1,j}^n + \left(1 + \frac{\Delta x_i - \Delta x_{i-1}}{\Delta x_i + \Delta x_{i-1}} \right) (u_1)_{i-1,j}^n \right] \\
&+ \frac{\Delta t^2}{\rho_{i,j}^0} \frac{2\mu}{\Delta y_j^2 + \Delta y_{j-1}^2} \left[\left(1 - \frac{\Delta y_j - \Delta y_{j-1}}{\Delta y_j + \Delta y_{j-1}} \right) (u_1)_{i,j+1}^n + \left(1 + \frac{\Delta y_j - \Delta y_{j-1}}{\Delta y_j + \Delta y_{j-1}} \right) (u_1)_{i,j-1}^n \right] \\
&+ \frac{\Delta t^2}{\rho_{i,j}^0} \frac{\lambda + \mu}{(\Delta x_i + \Delta x_{i-1})(\Delta y_j + \Delta y_{j-1})} \left((u_2)_{i+1,j+1}^n - (u_2)_{i-1,j+1}^n - (u_2)_{i+1,j-1}^n + (u_2)_{i-1,j-1}^n \right).
\end{aligned}$$

The corresponding stencil is illustrated in Figure 3.

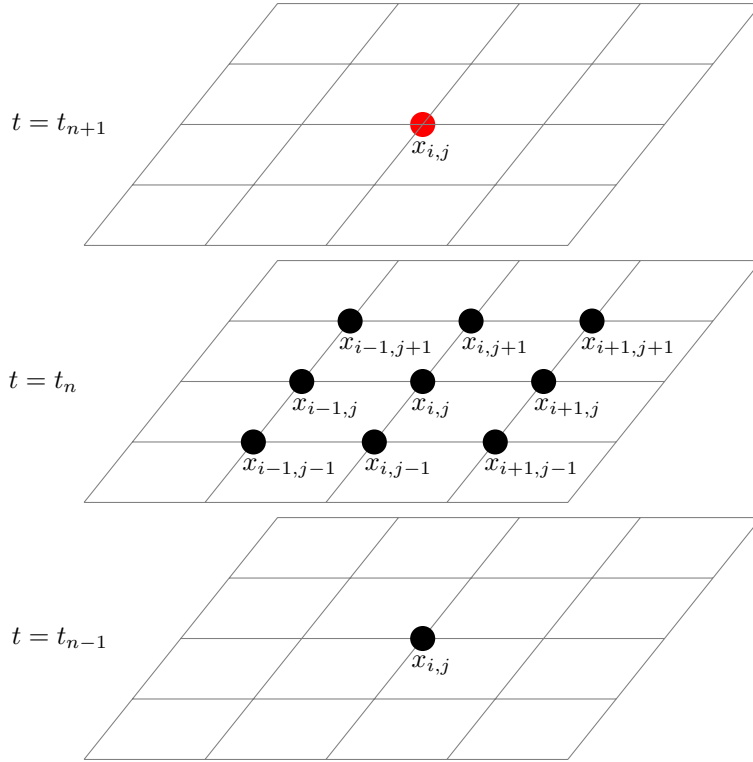


Figure 3: We illustrate the stencil for our numerical scheme. For the update of the values at node $x_{i,j}$ from $t_n \rightarrow t_{n+1}$, we have to provide information about the values at the other marked nodes.

For the first time step, the (discrete) initial condition needs to be inserted

$$(u_k)_{i,j}^{-1} = (u_k)_{i,j}^1 - 2\Delta t \vartheta^1(x_{i,j}) \quad \text{for } k = 1, 2.$$

The stencil for the spatial discretization has nine nodes. Since we are inspired by medical applications and a thorax is a possible specimen to be studied, we might deal with curved domains. For curved domains at the boundary, for the update scheme there is a node, which is not available to the stencil, see Figure 4. Hence, we need to use an interpolation method.

For reasons of stability, we want to maintain the stencil. We call the missing node a ghost node that needs to have a value assigned to it, and we denote h the quantities given at every node. The indices of the nodes are given in Figure 4. A second-order approach is the following one for the components $k = 1, 2$:

$$(h_k)_{\text{ghost}} = (h_k)_0 + \frac{(h_k)_{\text{aux}} - (h_k)_0}{(x_k)_{\text{aux}} - (x_k)_0} ((x_k)_{\text{ghost}} - (x_k)_0)$$

where the auxiliary node on the continuous boundary is approximated by

$$x_{\text{aux}} = \frac{1}{2} ((x_1)_1 + (x_1)_0), \quad y_{\text{aux}} = \frac{1}{2} ((x_2)_2 + (x_2)_0) \quad \text{and} \\ (h_k)_{\text{aux}} = \frac{1}{2} ((h_k)_1 + (h_k)_2).$$

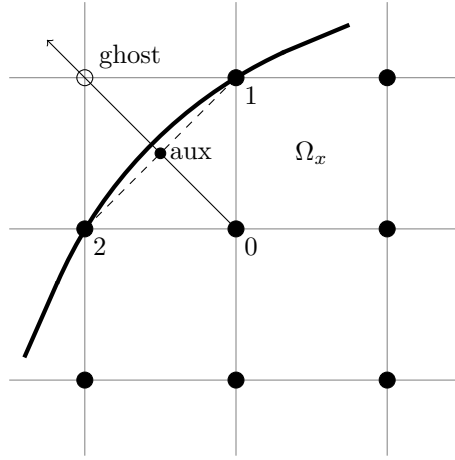


Figure 4: Illustration of the boundary: The nodes 1 and 2 lie directly on the continuous boundary, and their behaviour is prescribed by the Dirichlet data ψ . For the node 0, the stencil for the update scheme only can be applied with the help of an interpolation since the values of the ghost node are not available. The average of the values of the nodes 1 and 2 are used to create an auxiliary node which corresponds to a slightly ‘shifted’ boundary.

We use the CFL condition

$$\frac{\nu_x \Delta t}{\Delta x} + \frac{\nu_y \Delta t}{\Delta y} \leq 1,$$

where $\Delta x := \min \Delta x_i$ and $\Delta y := \min \Delta y_j$, in order to determine a suitable time step Δt . The maximal propagation speeds are bounded from above by $\nu_x, \nu_y \leq \sqrt{(\lambda + 2\mu)/\rho}$ with $\rho := \min \rho_{i,j}^0 > 0$.

5. Application in motion compensation. We evaluate the motion estimation approach on simulated CT data. For this purpose, we consider a thorax phantom representing

a cross-section of a chest, see Figure 5 left. Following from [11], its respiratory motion is modelled by an affine deformation, more precisely by

$$\Phi(t, x) = \begin{pmatrix} s(t)^{-1} & 0 \\ 0 & s(t) \end{pmatrix} \left(x - \begin{pmatrix} 0.44 \cdot (s(t) - 1) \\ 0 \end{pmatrix} \right)$$

with $s(t) = 0.05 \cdot \cos(0.04 \cdot t) + 0.95$. The deformation during one breathing cycle is illustrated in the sequence of pictures in Figure 5. The phantom represents a cross-section of a simulated chest.

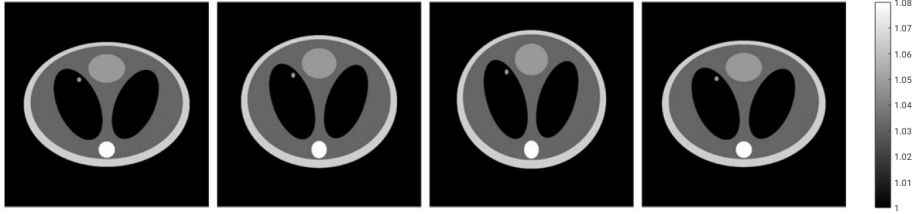


Figure 5: Cross-section of the numerical phantom during one cycling breath. The first image corresponds to the reference state, the second and third image correspond to the body after a quarter and after one half of a breathing cycle, respectively. The fourth image illustrates the body after one period when the initial configuration is reached again.

The Radon data of this dynamic object are computed for 660 source positions, uniformly distributed over the upper half sphere, and 451 discrete detector points uniformly distributed over $[-1, 1]$ (since the support of the phantom is contained in the unit disk at all time instances). Our reconstructions and - later on - all simulations of the PDE are run on a 257×257 grid.

If one does not take into account that the object was moving during data acquisition and applies a static reconstruction algorithm to the dynamic data, an image of poor quality with motion artefacts such as blurring, streaking etc. is obtained, see Figure 6(B). This motivates the need for motion compensation and hence motion estimation strategies.

As motion compensation algorithm, we use the strategy specified in Section 2.3 with the Gaussian function as low-pass filter. The result of this algorithm with exact motion information Φ is shown in Figure 6(C). We observe that all components are indeed correctly reconstructed without motion artefacts, i.e. the motion is well compensated for, and in accordance to [18], we obtain a good approximation to the original initial state, cf. Figure 6(A). However, in practice, the exact motion information is typically unknown.

Thus, our goal is now to evaluate our proposed motion estimation strategy, i.e. the (discrete) deformation fields Φ_t are computed by solving the Navier-Cauchy equation with available initial and boundary data. Since the reconstruction part of the algorithm is already established in the literature, for more details about the reconstruction quality, stability regarding noise in the Radon data and the effectiveness of this part we refer to [16, 18]. In particular, its regularizing property in order to cope with noisy measurements has been illustrated with examples from CT [16] and photoacoustic tomography [18].

As discussed in Remark 5, having only prescribed boundary data of a periodic and elastic

movement, the Navier-Cauchy equation is a basic model to approximate the motion of the internal thorax.

First, we discuss the initial data corresponding to the initial density distribution $\hat{\rho}$. As discussed in Remark 3.2, this initial parameter is strongly linked to the searched-for initial state function f_0 which is why we propose to use a simplified prior instead. The one used for our simulation is shown in the first image of Figure 7. This prior only distinguishes between spine and soft tissue, where the respective values are initialized with standard values $\hat{\rho} = 1.85 \cdot 10^3 \text{ kg/m}^3$ for the spine and $\hat{\rho} = 1.05 \cdot 10^3 \text{ kg/m}^3$ for the rest. This is indeed a reasonable prior in practice since the only component considered in the interior - the spine - typically does not move, so it can be extracted from a static reconstruction, cf. Figure 6(B). This prior can optionally be improved by an iteration between the motion estimation with given $\hat{\rho}$ and image reconstructions, which then update $\hat{\rho}$ again.

Finding realistic values for the Lamé-coefficients of human tissue is a research topic by itself. It is hard to quantify them and they differ depending on the study [47]. We assume a uniform motion behavior of all (soft) tissues and restrict ourselves to one set of values for the whole thorax. The coefficients are averaged to $\lambda = 3.46 \text{ kPa}$ and $\mu = 1.48 \text{ kPa}$. This simplifying assumption is reasonable for a first approach and also yields promising results in combination with the reconstruction algorithm.

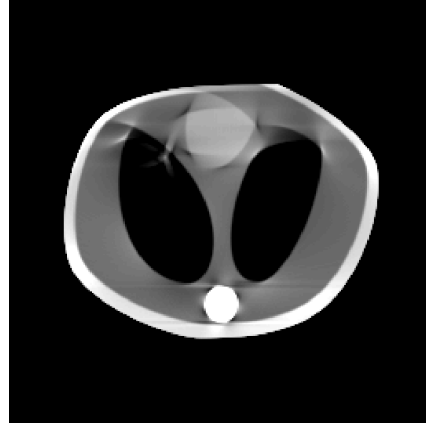
Regarding the boundary data, we test several configurations. First, we use the exact analytical positions of the boundary. The result for solving the respective PDE as described in Section 4 is illustrated in Figure 7. Then, incorporating its solution as motion information in our dynamic reconstruction algorithm provides the reconstruction result shown in Figure 6(D). Furthermore, in Figure 6(E) a sample of noise uniformly distributed in $[-0.003, 0.003]$ was added to the Radon data in order to illustrate stability of the motion compensation algorithm. In both cases the motion of the phantom is well compensated for and the small tumour is clearly visible. This shows that determining deformation fields by solving the Navier-Cauchy equation constitutes a valuable motion estimation strategy.

In practice, the boundary positions might be determined by attaching markers at the surface of the object. If these positions are determined by measurements, they will be subject to small measurement errors. Thus, in order to test stability with respect to the boundary data, we next add a sample of noise to the (analytical) boundary positions. The noise is generated as normal distribution around 0 with standard deviation 0.1 and 0.25, respectively. In Figure 8 we see that the reconstruction near the boundary is affected. More precisely, due to the inexact boundary positions, the boundary in the reconstruction appears fuzzy. However, the motion in the interior of the phantom is still well compensated for. All interior components, which correspond to the relevant searched-for information, including the small tumour, are still clearly recognizable, in particular in comparison to the static reconstruction, cf. Figure 6(B).

Further, we test the performance of the method if only a few discrete boundary positions are given. The motivation behind this experiment is that, in practice, only a limited number of markers can be attached to the surface of the object. To this end, we prescribe only 32 (and 16, respectively) grid nodes on the boundary. Between these nodes, we apply a linear interpolation. The results are displayed in Figure 9. We obtain some artefacts since the round shape of the thorax is replaced by a polygon due to the interpolation. However, as in the case of noisy boundary data, the deformation fields obtained by solving the PDE still provide sufficient information on the motion to compensate for it in the interior and to provide an image showing clearly all inner components including the small tumour.



(a) Original phantom



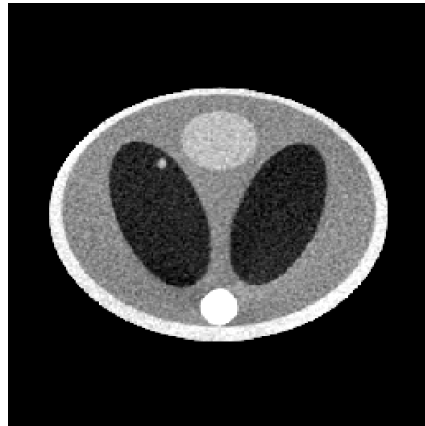
(b) Static reconstruction.



(c) Dynamic reconstruction with exact motion information.



(d) Dynamic reconstruction with motion information from solving the PDE with analytical boundary data.



(e) Dynamic reconstruction from noisy Radon data with motion information from solving the PDE with analytical boundary data.

Figure 6: Static and dynamic reconstruction results of the initial state function.

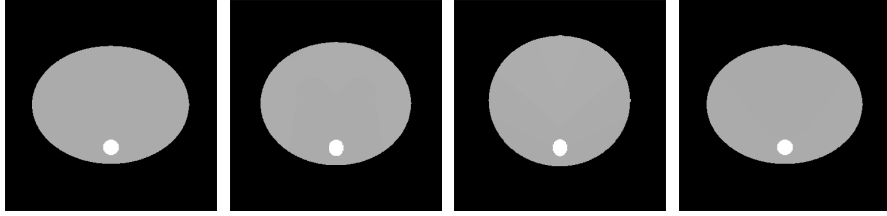
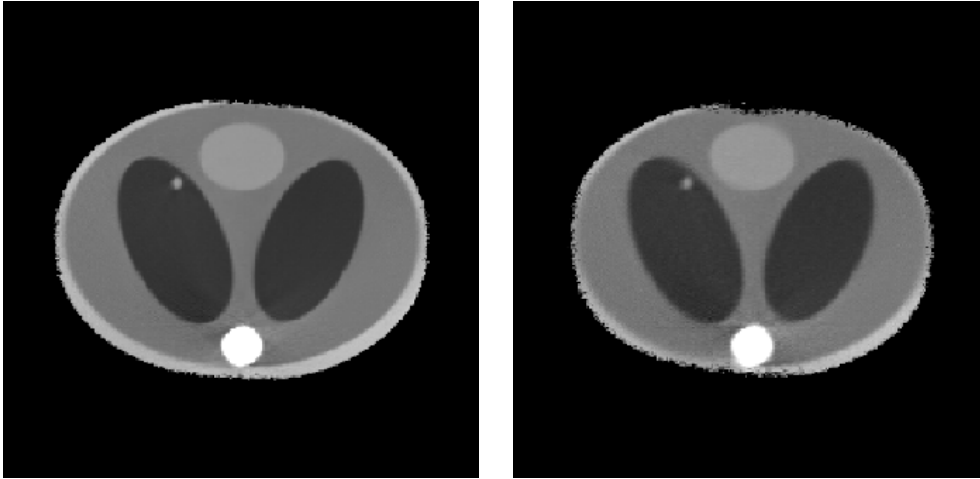


Figure 7: Illustration of the numerical solution of the Navier-Cauchy equation with analytical boundary data. The initial density distribution used for solving the Navier-Cauchy equation is given in the first image. The second, third and fourth image correspond to the configurations after a quarter, after one half and after a full period of the breathing cycle.



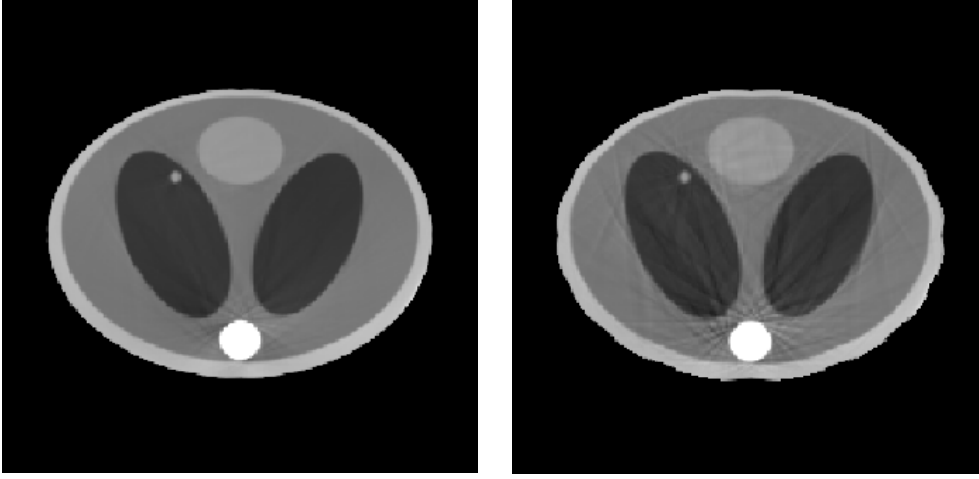
(a) Result for noisy boundary data with standard deviation 0.1.

(b) Result for noisy boundary data with standard deviation 0.25.

Figure 8: Dynamic reconstruction with motion information from solving the PDE with noisy boundary data.

6. Conclusions and Outlook. This article provides a proof-of-concept for a motion estimation strategy in dynamic imaging, where the Navier-Cauchy equation serves as a mathematical model for small elastic deformations. To this end, we decoupled the tasks of motion estimation and image reconstruction, i.e. the Navier-Cauchy equation is solved prior to the reconstruction step using suitable and realistic initial and boundary data. Then the calculated deformation fields are incorporated into an analytic dynamic reconstruction algorithm. Our numerical results on a thorax phantom undergoing respiratory motion illustrate that this approach can significantly reduce motion artefacts in the respective images. In particular, we discussed available boundary data and illustrated their affect on the reconstruction result.

We illustrated the usefulness and practicability of our idea: observe the thorax's bound-



(a) Result for 32 prescribed boundary nodes. (b) Result for 16 prescribed boundary nodes.

Figure 9: Dynamic reconstruction results with motion information from solving the PDE with only a small number of boundary nodes.

ary, find an estimation of the thorax's motion by numerically solving a PDE, and use this approximate motion data in the reconstruction algorithm. In our numerical results, we see that the reconstruction is improved a lot compared to a static reconstruction, even by using this basic motion estimation.

In this proof-of-concept study, all simulations were run on modern desktop computers. The total computational time is the sum of time needed to solve the PDE plus to solve the inverse problem. Concerning the algorithm for the inverse problem: due to its construction, the complexity of the motion compensation algorithm is the same as for standard filtered backprojection algorithms, described for instance in [35]. The implementation of the numerical scheme for the PDE was not tuned regarding efficiency, so simulation for the motion data took hours. However, in work in progress we have more elaborated techniques at hand, which significantly reduce computational costs for solving the PDE. We expect that we can then run a simulation within a few minutes on a laptop computer, this includes the time for solving the inverse problem. Thus it should be feasible to use our method in applications.

In future work, a more realistic biomechanical material law than Hooke's law will be considered. More elaborated numerical schemes will then be implemented for more specific studies, also regarding computation times. A worthwhile approach might be to minimize the distance between observed and simulated displacements in combination with solving an initial boundary value problem. Additionally, more importance will be attached to the specific behavior of different parts of the thorax. For instance, as the heart follows its own cycle, it effects the lungs' motion and its influence would also be interesting to consider.

So far, we have decoupled the suggested motion estimation and compensation approach: For estimating the deformation fields, we included a rough prior on the initial density distribution $\hat{\rho}$. This prior was then improved by incorporating the computed motion information in the image reconstruction step. The next step is to study the joint parameter identification

problem, i.e. to address the challenging task of recovering $\hat{\rho}$ directly from (3.1) with the usual boundary conditions and the data constraint $\mathcal{A}_\Phi \hat{\rho} = g$.

Acknowledgments. The first and second authors are supported by the Deutsche Forschungsgemeinschaft under grant HA 8176/1-1. The third and fourth authors want to thank Matteo Semplice for fruitful discussions.

REFERENCES

- [1] S. S. Antman, *Nonlinear Problems of Elasticity (Second Edition)*, Springer, New York, 2004.
- [2] C. Blondel, R. Vaillant, G. Malandain and N. Ayache, 3d tomographic reconstruction of coronary arteries using a precomputed 4d motion field, *Physics in Medicine and Biology*, **49** (2004), 2197–2208.
- [3] V. Boutchko R. Rayz, N. Vandehey, J. O’Neil, T. Budinger, P. Nico and W. Moses, Imaging and modeling of flow in porous media using clinical nuclear emission tomography systems and computational fluid dynamics, *Journal of Applied Geophysics*, **76** (2012), 74–81.
- [4] M. Burger, H. Dirks, L. Frerking, A. Hauptmann, T. Helin and S. Siltanen, A variational reconstruction method for undersampled dynamic x-ray tomography based on physical motion models, *Inverse Problems*, **33** (2017), 124008.
- [5] M. Burger, H. Dirks and C.-B. Schönlieb, A variational model for joint motion estimation and image reconstruction, *SIAM Journal on Imaging Sciences*, **11** (2018), 94–128.
- [6] C. Chen, B. Gris and O. Öktem, A new variational model for joint image reconstruction and motion estimation in spatiotemporal imaging, *SIAM J. Imaging Sciences*, **12** (2019), 1686–1719.
- [7] C. Chen and W. von Wahl, Das rand-anfangswertproblem für quasilineare wellengleichungen in sobolevräumen niedriger ordnung, *Journal für die reine und angewandte Mathematik*, 77–112.
- [8] J. Chung, A. K. Saibaba, M. Brown and E. Westman, Efficient generalized golub-kahan based methods for dynamic inverse problems, *Inverse Problems*, **34** (2018), 024005.
- [9] J. Chung and L. Nguyen, Motion estimation and correction in photoacoustic tomographic reconstruction, *SIAM J. Imaging Sci.*, **10** (2017), 216–242.
- [10] P. G. Ciarlet, *Mathematical Elasticity, Vol. I: Three-Dimensional Elasticity*, NH, 1988.
- [11] C. Crawford, K. King, C. Ritchie and J. Godwin, Respiratory compensation in projection imaging using a magnification and displacement model, *IEEE Transactions on Medical Imaging*, **15** (1996), 327–332.
- [12] L. Desbat, S. Roux and P. Grangeat, Compensation of some time dependent deformations in tomography, *IEEE Transactions on Medical Imaging*, **26** (2007), 261–269.
- [13] J. Fitzgerald and P. Danias, Effect of motion on cardiac spect imaging: Recognition and motion correction, *Journal of Nuclear Cardiology*, **8** (2001), 701–706.
- [14] F. Gigengack, L. Ruthotto, M. Burger, C. Wolters, X. Jiang and K. Schäfers, Motion correction in dual gated cardiac pet using mass-preserving image registration, *IEEE Trans. Med. Imag.*, **31** (2012), 698–712.
- [15] E. Gravier, Y. Yang and M. Jin, Tomographic reconstruction of dynamic cardiac image sequences, *IEEE Transactions on Image Processing*, **16** (2007), 932–942.
- [16] B. N. Hahn, Efficient algorithms for linear dynamic inverse problems with known motion, *Inverse Problems*, **30** (2014), 035008, 20.
- [17] B. N. Hahn, Motion estimation and compensation strategies in dynamic computerized tomography, *Sensing and Imaging*, **18** (2017), 1–20.
- [18] B. N. Hahn and M.-L. Kienle Garrido, An efficient reconstruction approach for a class of dynamic imaging operators, *Inverse Problems*, **35** (2019), 094005.
- [19] B. N. Hahn, M.-L. Kienle Garrido and E. T. Quinto, Microlocal properties of dynamic Fourier integral operators, in *Time-dependent Problems in Imaging and Parameter Identification* (eds. B. Kaltenbacher, T. Schuster and A. Wald), Springer Verlag, to appear.
- [20] B. Hahn, Reconstruction of dynamic objects with affine deformations in dynamic computerized tomography, *J. Inverse Ill-Posed Probl.*, **22** (2014), 323–339.
- [21] B. N. Hahn and E. T. Quinto, Detectable singularities from dynamic radon data, *SIAM Journal on Imaging Sciences*, **9** (2016), 1195–1225.
- [22] L. Hörmander, *The analysis of linear partial differential operators IV: Fourier Integral Operators*, Springer, 2009.
- [23] T. Hughes, T. Kato and J. Marsden, Well-posed quasilinear second-order hyperbolic systems with applications to nonlinear elastodynamics and general relativity, *Arch. Rational Mech. Anal.*, **63**

- (1977), 273–294.
- [24] A. Isola, A. Ziegler, T. Koehler, W. Niessen and M. Grass, Motion-compensated iterative cone-beam ct image reconstruction with adapted blobs as basis functions, *Physics in Medicine and Biology*, **53** (2008), 6777–6797.
 - [25] J. Kastner, B. Plank and C. Heinzl, Advanced x-ray computed tomography methods: High resolution ct, phase contrast ct, quantitative ct and 4dct, in *Digital Industrial Radiology and Computed Tomography (DIR 2015)*, Ghent, Belgium, 2015.
 - [26] A. Katsevich, An accurate approximate algorithm for motion compensation in two-dimensional tomography, *Inverse Problems*, **26** (2010), 065007, 16.
 - [27] A. Katsevich, A local approach to resolution analysis of image reconstruction in tomography, *SIAM J. Appl. Math.*, **77** (2017), 1706–1732.
 - [28] A. Katsevich, M. Silver and A. Zamyatin, Local tomography and the motion estimation problem, *SIAM J. Imaging Sci.*, **4** (2011), 200–219.
 - [29] S. Kindermann and A. Leitão, On regularization methods for inverse problems of dynamic type, *Numerical Functional Analysis and Optimization*, **27** (2006), 139–160.
 - [30] V. P. Krishnan and E. T. Quinto, Microlocal Analysis in Tomography, in *Handbook of Mathematical Methods in Imaging* (ed. O. Scherzer), Springer Verlag, 2015.
 - [31] D. Le Bihan, C. Poupon, A. Amadon and F. Lethimonnier, Artifacts and pitfalls in diffusion mri, *Journal of Magnetic Resonance Imaging*, **24** (2006), 478–488.
 - [32] J. Liu, X. Zhang, X. Zhang, H. Zhao, Y. Gao, D. Thomas, D. Low and H. Gao, 5d respiratory motion model based image reconstruction algorithm for 4d cone-beam computed tomography, *Inverse Problems*, **31** (2015), 115007.
 - [33] W. Lu and T. R. Mackie, Tomographic motion detection and correction directly in sinogram space, *Tomographic motion detection and correction directly in sinogram space*, **47** (2002), 1267–1284.
 - [34] D. Manke, K. Nehrke and P. Börnert, Novel prospective respiratory motion correction approach for free-breathing coronary mr angiography using a patient-adapted affine motion model, *Magnetic Resonance in Medicine*, **50** (2003), 122–131.
 - [35] F. Natterer, *The mathematics of computerized tomography*, B. G. Teubner, Stuttgart, 1986.
 - [36] F. Natterer and F. Wübbeling, *Mathematical methods in image reconstruction*, SIAM Monographs on Mathematical Modeling and Computation, Society for Industrial and Applied Mathematics (SIAM), Philadelphia, PA, 2001.
 - [37] R. Otazo, E. Candès and D. Sodickson, Low-rank plus sparse matrix decomposition for accelerated dynamic mri with separation of background and dynamic components, *Magnetic Resonance in Medicine*, **73** (2015), 1125–1136.
 - [38] S. Rabieniaharatbar, Invertibility and stability for a generic class of radon transforms with application to dynamic operators, *Journal of Inverse and Ill-Posed Problems*, **27** (2018), 469–486.
 - [39] M. Reyes, G. Malandain, P. Koulibaly, M. González-Ballester and J. Darcourt, Model-based respiratory motion compensation for emission tomography image reconstruction, *Physics in Medicine and Biology*, **52** (2007), 3579–3600.
 - [40] U. Schmitt and A. Louis, Efficient algorithms for the regularization of dynamic inverse problems: I. theory, *Inverse Problems*, **18** (2002), 645–658.
 - [41] U. Schmitt, A. Louis, C. Wolters and M. Vauhkonen, Efficient algorithms for the regularization of dynamic inverse problems: II. applications, *Inverse Problems*, **18** (2002), 659–676.
 - [42] L. Shepp, S. Hilal and R. Schulz, The tuning fork artifact in computerized tomography, *Computer Graphics and Image Processing*, **10** (1979), 246–255.
 - [43] R. M. Temam and A. M. Miranville, *Mathematical Modeling in Continuum Mechanics (Second Edition)*, Cambridge University Press, New York, 2005.
 - [44] F. Trèves, *Introduction to Pseudodifferential and Fourier Integral Operators*, Volume 2: Fourier Integral Operators, Plenum Press, New York and London, 1980.
 - [45] G. Van Eyndhoven, J. Sijbers and J. Batenburg, Combined motion estimation and reconstruction in tomography, *Lecture Notes in Computer Science*, **7583** (2012), 12–21.
 - [46] V. Van Nieuwenhove, J. De Beenhouwer, T. De Schryver, L. Van Hoorebeke and J. Sijbers, Data-Driven Affine Deformation Estimation and Correction in Cone Beam Computed Tomography, *IEEE Transactions on Image Processing*, **26** (2017), 1441–1451.
 - [47] R. Werner, *Strahlentherapie atmbewegter Tumoren*, Springer Vieweg, Wiesbaden, 2013.
 - [48] H. Yu and G. Wang, Data consistency based rigid motion artifact reduction in fan-beam ct, *IEEE Transactions on Medical Imaging*, **26** (2007), 249–260.